

# Forcing function and volumetric flow field estimation for a cylinder undergoing VIV

Jeffrey McClure<sup>1\*</sup>, Chris Morton<sup>2</sup>, Serhiy Yarusevych<sup>1</sup>

<sup>1</sup> University of Waterloo, Mechanical & Mechatronics Engineering, Waterloo, Canada

<sup>2</sup> University of Calgary, Mechanical & Manufacturing Engineering, Calgary, Canada

\* jejmccclu@uwaterloo.ca

## Abstract

The time-resolved forcing on a finite-span cylindrical body is estimated from planar TR-PIV measurements based on a pseudo-instantaneous reconstruction of the flow field in three-dimensions surrounding the body. The method is applied to a stationary cylinder in cross flow, and two forced vibration cases corresponding to  $2S$  and  $2P_0$  modes of vortex-induced vibrations. PIV-based pressure and loading measurements are obtained from solution of a Poisson equation and momentum balance in horizontal planar measurements normal to the cylinder axis, and their coherent fluctuations are related to the phase of the primary shedding instability. These relations are then leveraged with estimates of the instantaneous spanwise distribution of shedding phase derived from vertical planar measurements parallel with the cylinder axis through correlation of shared streamwise velocity signals between the horizontal and vertical planar measurements at any given spanwise location. The resulting estimates of instantaneous fluid forcing are compared to simultaneously acquired force balance data, and are shown to capture the low frequency modulation of the fluctuating lift force associated with shedding phase variation along the span for the uniform stationary cylinder. However, for the oscillating cylinder cases, the reconstruction along the span suffers from errors in phase identification due to spanwise inhomogeneity of the flow. Instead, for the oscillating cylinder cases, the sectional fluctuating lift coefficients agree favourably with the reference force balance data.

## 1 Introduction

Within the wide-spread deployment of Particle Image Velocimetry (PIV) and Particle Tracking Velocimetry (PTV) systems for application in industrial and laboratory settings, it is of interest to extract time-resolved load estimates from such measurements Rival and van Oudheusden (2017). There are a few candidate formulations to choose from for evaluating forcing from velocimetry data: (i) the pressure-velocity formulation (Unal et al., 1997; Wu et al., 2005; McClure and Yarusevych, 2019) (i.e., momentum methods), (ii) the vorticity-velocity formulation (Noca et al., 1999; Guissart et al., 2017; Graham et al., 2017; Limacher et al., 2018) (i.e., impulse methods), and (iii) the Lagrangian drift volume formulation (Dabiri, 2005; McPhaden and Rival, 2018). For flows with significant contributions from added mass and vortex force components, a complete force estimate can only be obtained from the momentum and impulse methods. The classical momentum formulation is selected for consideration in the current study, due to its characteristically lower error sensitivity (Noca et al., 1999; Limacher et al., 2019) compared to impulse methods for finite domains. In addition, the concomitant resolution of the pressure field facilitates advanced diagnostics for applications involving flexible structures and aeroacoustics.

A limitation of time-resolved PIV-based loading estimates is their application in three-dimensional flows with salient dynamics occurring outside the PIV measurement plane or volume. Since, in general, the flow completely surrounding the body must be resolved for time-resolved force estimation, this poses an experimental challenge for both resolution and illumination. Specifically, tomographic camera set-ups have limited ability to resolve the flow near highly curved geometries, and mitigation of optical shadowing, encountered when the measurements domain encompasses a solid body, requires a drastic increase in complexity of the measurement. In addition, the light budget limitations often restrict the size of the measurement volume, making illuminating the flow surrounding the entire immersed body infeasible in most cases. Spoelstra et al. (2019) circumvent this issue for evaluation of time-resolved drag force by utilizing a single measurement

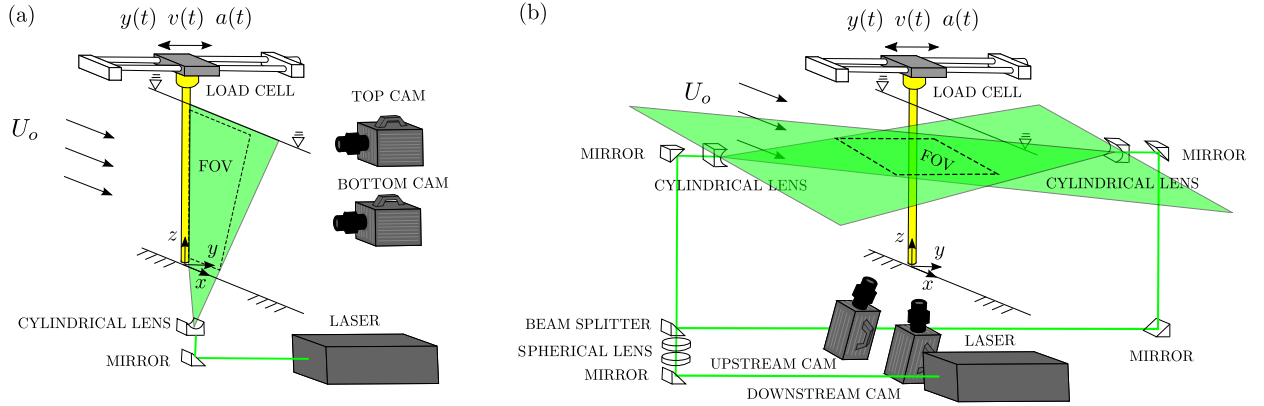


Figure 1: Experimental configuration for (a) vertical plane (x-z) and (b) horizontal plane (x-y) PIV measurements.

volume downstream of a cyclist, aimed at capturing the entire extent of the time-resolved evolution of the trailing wake permitting the use of a simplified control volume analysis.

The approach in this study, is primarily aimed at measuring the fluctuating lift force utilizes a pseudo-instantaneous three-dimensional flow reconstruction technique derived from a minimum of two independent time-resolved, planar Particle Image Velocimetry (TR-PIV) measurements to estimate time-resolved fluid pressure and loads for a stationary and oscillating cylinder in cross flow at a Reynolds of approximately 4100. The study serves as a validation case of the proposed methodology, with the TR-PIV measurements accompanied by reference force balance data to benchmark the accuracy of the proposed methods.

## 2 Experimental Methodology

Experiments were performed in a closed-loop water tunnel facility at the University of Calgary. The tunnel test section width and free surface height were  $0.385m$  and  $0.431m$ , respectively. The free-stream velocity was set to  $U_0 = 0.21m/s$ , and was monitored by a Dynasonics TFX ultrasonic flow meter. The experimental configuration is depicted in figure 1. A cylinder model was mounted vertically on an actuated platform capable of linear motion over a range of amplitudes ( $A$ ) and frequencies ( $f$ ) in the cross-flow direction to replicate one-degree-of-freedom Vortex-Induced Vibrations (VIV). The cylinder model had diameter  $D = 19.05mm$ , resulting in solid blockage of 5%, and was made hollow to enhance PIV laser light penetration and minimize inertial loading during motion, with a total mass of  $0.167$  kg. The aspect ratio of the immersed portion of the cylinder was  $L/D = 22.62$ , and the free end of the cylinder extended to within  $1$  mm of the test section floor. The Reynolds number based on cylinder diameter was approximately 4100. Three cases were investigated: (i) a stationary cylinder, (ii) forced VIV at normalized amplitude  $A^* = A/D = 0.45$  and wavelength  $\lambda^* = U_0/fD = 5$  resulting in 2S shedding, and (iii) forced VIV at  $A^* = 0.8$  and  $\lambda^* = 7$  resulting in  $2P_0$  shedding (Morse and Williamson, 2009). Time-resolved, two-component, planar PIV-measurements in  $x-y$  and  $x-z$  planes are obtained in sync with force and cylinder position measurements from a load cell and encoder, respectively.

The sinusoidal trajectory of the cylinder is actuated by a motorized traverse above the free surface of the water channel. The traverse is driven by a digital brushless servomotor (ClearPath MCVC-2341P) through a timing belt attached to a moving carriage mounted between two v-slot linear rails aligned in the transverse direction, ensuring motion in only one degree-of-freedom. The position of the carriage is monitored by an optical encoder with 800 counts per revolution resulting in a resolution of  $0.002D$  in position measurement. A homing procedure was used to consistently centre the cylinder position in the test section with an uncertainty within  $\pm 0.016D$ . Coaxially mounted to the bottom of the carriage are the load cell and acrylic cylinder model. A detailed description of the control system implemented to follow the input sinusoidal trajectories is included in Riches and Morton (2018). In the current work, the desired trajectory is prescribed as a sinusoid with a given amplitude and frequency  $y = A \sin(2\pi ft)$ .

Instantaneous forces were measured using an ATI Mini40 six-component load cell. The load cell force resolution is  $0.005N$ . In the oscillating cylinder cases, the inertial force on the load cell associated with accelerating/decelerating the cylinder model assembly must be quantified and subtracted from transverse lift

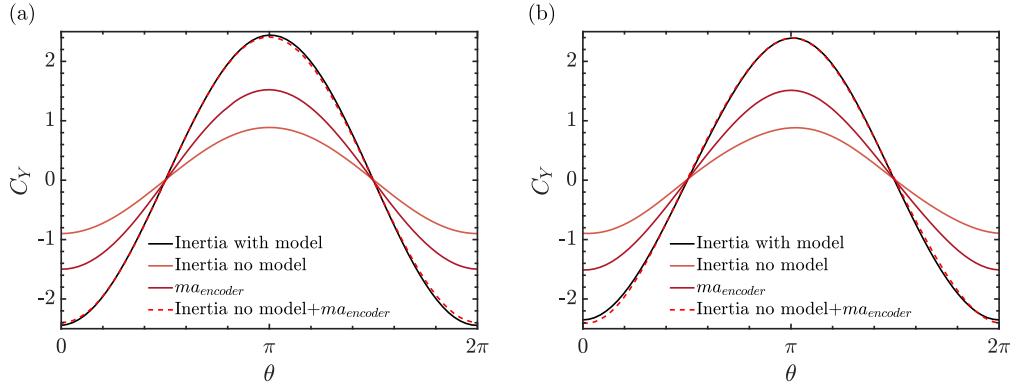


Figure 2: Phase-averaged inertial lift force subtraction for oscillating cylinder cases (a)  $A^* = 0.45$  and  $\lambda^* = 5.0$  and (b)  $A^* = 0.8$  and  $\lambda^* = 7.0$ .

force measurements. To do so, the prescribed motion for the two oscillating cases was repeated in air, and the resulting filtered lift data was phase averaged using the phase of the cylinder position computed by the Hilbert transform (Khalak and Williamson, 1999) providing an estimate for the phase-averaged inertial force (black line, figure 2). The result was then subtracted from the forces obtained in the current experiments based on the phase of the cylinder position. The inertial subtraction was further validated by repeating the prescribed motion in air with the cylinder model detached from the load cell. The resulting phase averaged inertial force when added to the additional inertial force computed by the measured mass of the cylinder model undergoing acceleration measured by the second derivative of the filtered encoder data ( $ma_{encoder}$ ) matches the previously obtained inertial subtraction with the entire assembly actuated (figure 2). The correspondence of the two signals suggests no secondary inertial effects, e.g., due to deflection of the cylinder model, are significant.

Velocity measurements were obtained in six independent planes using two-component, time-resolved PIV, comprising of three vertical  $x-z$  planes (figure 1a) at transverse positions  $y/D = 0, 0.5$ , and  $1.0$ , and three horizontal  $x-y$  planes (figure 1b) at spanwise positions  $z/D = 5, 11.9$  and  $17.7$ . The flow was seeded with  $10\mu m$  hollow glass spheres, with specific gravity  $1.05$ , illuminated by a high repetition rate Photonics DM30 Nd:YLF laser. Particle images were acquired with two  $2560 \times 1600$  px Phantom Miro 340 high-speed cameras equipped with  $60mm$  lenses. Scheimpflug adapters were affixed to the lenses for the horizontal plane measurements, and the cameras rotated  $20deg$  from the vertical axis to facilitate resolution of the velocity field surrounding the entire cylinder surface. For each measurement plane and set of parameters,  $10000$  images were acquired at  $f_{acq} = 400Hz$  in single frame mode, approximately  $200$  times the Strouhal shedding frequency of the stationary cylinder. The velocity fields were processed in DaVis 8.4.0 using an iterative multigrid algorithm with window deformation at a final interrogation window size of  $24 \times 24$  px with  $75\%$  overlap. Erroneous vectors were eliminated by employing a median temporal filter over a sliding kernel of  $7$  velocity fields. After stitching the resulting vector fields from two cameras in a minor  $< 0.5D$  overlap region with a linear weighting factor, the final  $x-y$  Field of View (FOV) was  $-3.6 < x/D < 3.6$ ,  $-1.9 < y/D < 1.9$ , and  $x-z$  FOV was  $0 < x/D < 4.0$ ,  $0.1 < z/D < 20.2$ , with a vector pitch of  $0.55mm$  ( $0.029D$ ) and  $0.31mm$  ( $0.016D$ ) in the  $x-z$  and  $x-y$  planes, respectively.

The PIV laser Q-switch, encoder, and load cell force signals were acquired simultaneously at  $f_{acq} = 50$  kHz with an Advantech PCI1716L DAQ card. The encoder, and force balance signals were synchronized with the PIV velocity measurements through resampling the acquired data at the mid point between rising edges of the Q-switch corresponding to the timing of laser pulses. In the oscillating cylinder cases, data acquisition was initiated only after a minimum of  $10$  oscillation periods to ensure transients in the controls and flow dynamics did not influence the results.

## 2.1 Pressure and Force Estimation

A Poisson equation solver was employed to estimate pressure from the horizontal plane PIV measurements based on the numerical solution of equation 1 (e.g., Gurka et al., 1999).

$$\begin{aligned}
\nabla^2 p &= \nabla \cdot \left( -\rho \frac{D\mathbf{u}}{Dt} + \mu \nabla^2 \mathbf{u} \right), \quad \text{in } \Omega \\
\nabla p \cdot \mathbf{n} &= \left( -\rho \frac{D\mathbf{u}}{Dt} + \mu \nabla^2 \mathbf{u} \right) \cdot \mathbf{n}, \quad \text{on } \Gamma_i \\
p &= \frac{1}{2} \rho U_0^2 - \frac{1}{2} \rho (\bar{\mathbf{u}} \cdot \bar{\mathbf{u}} + \mathbf{u}' \cdot \mathbf{u}'), \quad \text{on } \Gamma_j
\end{aligned} \tag{1}$$

where  $\Gamma_i$  denotes boundary sections where Neumann boundary conditions are employed, setting the pressure gradient to that estimated from the Navier-Stokes equation, and  $\Gamma_j$  denotes boundary sections where the Dirichlet condition is employed, setting the pressure on the boundary using an extended form of the Bernoulli equation, valid for unsteady, irrotational flow with small mean velocity gradients (de Kat and van Oudheusden, 2012). Dirichlet condition were prescribed on the inflow boundary, where the flow was deemed approximately steady and irrotational for all cases, and Neumann conditions were prescribed on the remaining top, bottom, outflow boundaries and on a circular contour surrounding the cylinder. The contour around the cylinder had a diameter of  $1.2D$ , moving with the cylinder's position, in order to avoid amplified errors in near wall regions. For computation of sectional loads,  $\mathbf{F}_s = (F_x, F_y)$ , from the horizontal plane PIV measurements, a small control volume was selected surrounding the cylinder ( $-1.05 < x/D < 1.05$ ,  $-1.05 < y/D < 1.05$ ), to avoid regions of flow three-dimensionality. The mathematical formulation used is given in equation 2, which represents the approximate momentum balance for a planar control volume in three-dimensional flow (McClure and Yarusyevych, 2019), with viscous terms neglected.

$$\mathbf{F}_s = -\frac{d}{dt} \left( \int_S \rho \mathbf{u} dx dy \right) - \oint_l \rho \mathbf{u} (\mathbf{u} \cdot \mathbf{n}) dl + \int_S \rho \mathbf{u} (\nabla_{xy} \cdot \mathbf{u}) dx dy - \oint_l p \mathbf{n} dl \tag{2}$$

## 2.2 Pseudo-Instantaneous Three-Dimensional Reconstruction

Since planar PIV measurements are only capable of yielding sectional estimates of the flow induced loading, it is necessary to employ a reconstruction of the flow along the entire span of the cylinder model in order to accurately characterize the forcing. This is done by leveraging instantaneous, vertical plane PIV measurements located at a transverse position  $y = 0.5D$ . At each spanwise location, streamwise velocity data in the overlapping region between the vertical and horizontal plane PIV measurements is used to obtain an estimation for horizontal velocity fields, pressure fields, and sectional forces. This estimate is computed in two ways: (i) phase-averaging the horizontal plane measurements and correlating a line of streamwise velocity data at every spanwise location ( $z_k$ ) in the instantaneous vertical plane velocity field,  $u(x, y_v, z_k)$ , to identify the shedding phase at every spanwise position ( $\theta(z_k)$ ), and (ii) phase-averaging the horizontal plane measurements and projecting the same line of velocity data  $u(x, y_v, z_k)$  onto the horizontal POD-basis modes to estimate the temporal coefficients  $\{a_1(z_k), a_2(z_k), \dots\}$  at every spanwise position, the temporal coefficients can then be leveraged to compute the spanwise distribution of shedding phase.

To phase average the horizontal plane PIV measurements, Proper Orthogonal Decomposition (POD) is employed (Sirovich, 1987), which decomposes the velocity fields into deterministic spatial modes,  $\phi_i(x, y)$ , with corresponding time varying temporal coefficients,  $a_i(t)$ . Figures 3a-c plot the values of the first two temporal coefficients for the horizontal plane PIV data acquired at  $\hat{z} = 11.9$  for the stationary and oscillating cylinder cases. The first two temporal coefficients define the dominant dynamics of the primary shedding instability (Noack and Eckelmann, 2006), and the shedding phase can be identified by  $\theta = \text{atan} \sqrt{\lambda_2/\lambda_1} a_1/a_2$  (Oudheusden et al., 2005). Notably, figure 3a indicates a larger spread of temporal coefficient data for the stationary case, indicative of larger variations in planar wake dynamics, while the data for the oscillating cylinder case at  $A^* = 0.8$  and  $\lambda^* = 7.0$  has a slightly skewed distribution, presumably associated with the asymmetric wake dynamics for the observed  $2P_0$  shedding regime (Morse and Williamson, 2009). Once the shedding phase is identified for the acquired data during the horizontal plane PIV measurements, the corresponding phase averages of the velocity fields, pressure fields, PIV-based sectional loads, and total loads measured by the force balance are computed by binning the data into phase bins of  $\Delta\theta = 20^\circ$ .

To estimate the spanwise distribution of shedding phase from the vertical plane data at a given time, the streamwise velocity data at each spanwise position is either correlated with the corresponding line of data from each phase averaged streamwise velocity field, or the streamwise data is projected onto the

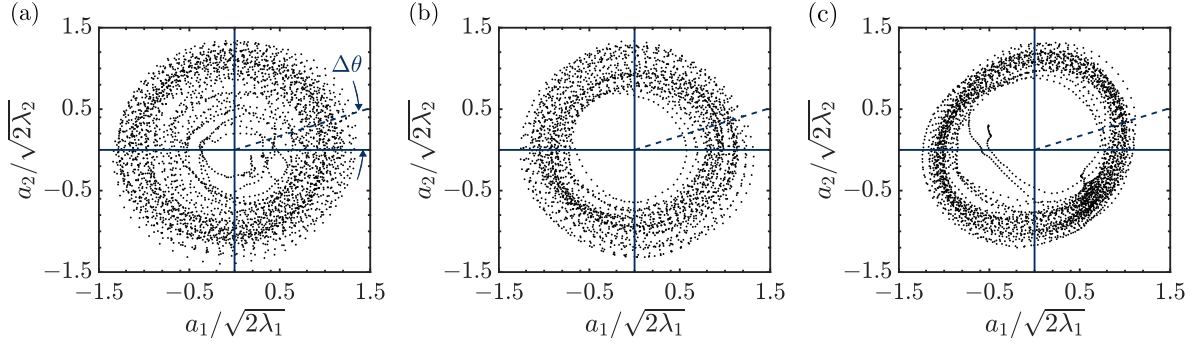


Figure 3: First two temporal coefficients of the POD for (a) stationary cylinder, (b) oscillating cylinder  $A^* = 0.45$ ,  $\lambda^* = 5.0$ , and (c) oscillating cylinder  $A^* = 0.8$ ,  $\lambda^* = 7.0$ .

corresponding line of data from the first two  $x - y$  plane POD modes ( $\phi_1(x, y_v)$ ,  $\phi_2(x, y_v)$ ) according to  $a_i(z_k, t) = \langle u(x, y_v, z_k), \phi_i(x, y_v) \rangle / \|\phi_i(x, y_v)\|^2$  to recover the temporal coefficients at each spanwise position which can be used to estimate the phase according to figure 3. For each case, a low order representation of the instantaneous flow field can be constructed according to  $u_{POD}(x, y, z, t) = \bar{u}(x, y, z) + \sum_i a_i(z, t) \phi_i(x, y)$  and  $u_{PA}(x, y, z, t) = u_\theta(x, y, z, \theta(z, t))$ , and the shedding phase along the span of the cylinder is used in conjunction with the phase-averaged sectional force data to estimate the total forcing.

### 3 Results

#### 3.1 Sectional Results

The main results of the analysis of the sectional PIV data acquired in the three horizontal planes at  $z/D = 5$ , 11.9, and 17.7 are summarized in figures 4, 5 and 6 for the stationary cylinder, oscillating cylinder in a 2S shedding regime, and oscillating cylinder in a 2P<sub>0</sub> shedding regime, respectively.

For the stationary cylinder, the total lift coefficient fluctuations are characteristically lower than the simultaneously acquired PIV-based estimates at  $\hat{z} = 11.9$ , and exhibit differences in phase with one another for the majority of the time sample. This result is expected since the spanwise variation of the shedding phase, unaccounted for in the sectional force estimates, act to reduce the resultant force experienced by the cylinder model. There are several instances where the sectional and total lift coefficient data show high correspondence in phase and amplitude (e.g.,  $0 < \hat{t} < 1.5$  and  $5 < \hat{t} < 6$  in figure 4a) indicating times when the phase of shedding happens to be highly correlated along the span. The resulting phase averages of instantaneous force measurements and PIV-based estimates based on the POD coefficient data in the sectional horizontal planes are shown in figure 4. The sectional lift coefficient data indicate the sectional fluctuating lift force increases as the measurement plane transverses downward in  $z$ .

For the oscillating case at  $A^* = 0.45$  and  $\lambda^* = 5.0$ , the total and sectional lift coefficient data are highly correlated in each horizontal plane and exhibit nearly matching amplitude (figure 5a,b). This is indicative of the lock-in of shedding phase along the span of the cylinder, typical for high amplitude vortex-induced vibrations (Bearman, 1984). The flow regime is denoted “2S” due to the shedding of two vortices per oscillation cycle (figures 5c,d), similar to the natural von Kármán wake for the stationary cylinder (figures 4c,d). For the oscillating case at  $A^* = 0.8$  and  $\lambda^* = 7.0$ , the total and sectional lift coefficient data are again highly correlated in each horizontal plane and exhibit nearly matching amplitude (figure 6a,b), though the minor deviations are more substantial than for the “2S” shedding case. Notably, the phase averaged estimates of the sectional loads exhibit variations in their peak location dependent on the spanwise position of the measurement plane (figure 6b). This indicates possible spanwise variations of the wake dynamics, on the average, though the correspondence of the phases of the sectional and total force coefficient data indicates that the shedding remains largely locked-in along the span.

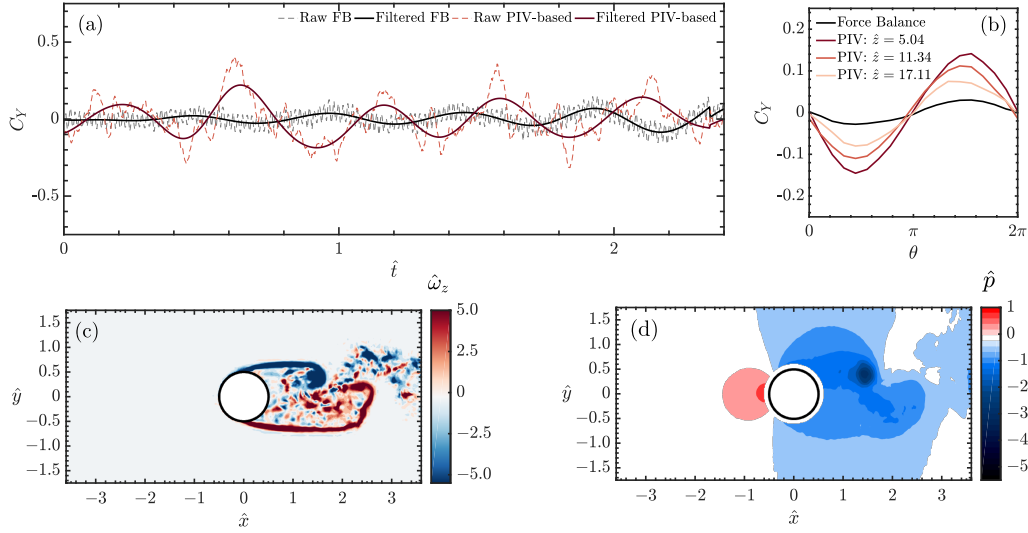


Figure 4: Sectional results for the stationary cylinder. (a) Total lift coefficient force balance data compared to PIV-based sectional lift coefficient data, (b) phase averages of these data for each spanwise plane investigated, (c) instantaneous spanwise vorticity field and (d) instantaneous PIV-based pressure field.

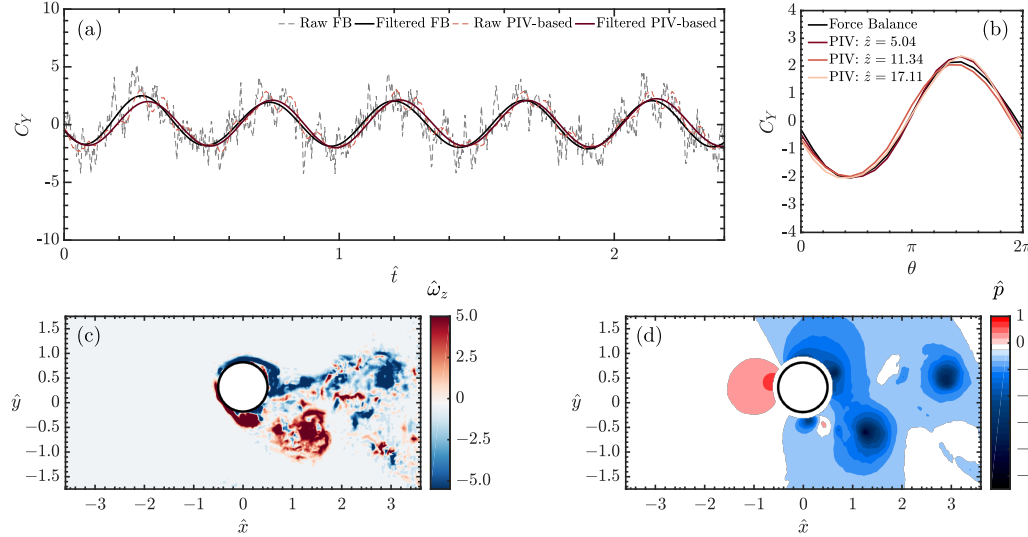


Figure 5: Sectional results for the oscillating cylinder at  $A^* = 0.45$ ,  $\lambda^* = 5.0$ . (a) Total lift coefficient force balance data compared to PIV-based sectional lift coefficient data, (b) phase averages of these data for each spanwise plane investigated, (c) instantaneous spanwise vorticity field and (d) instantaneous PIV-based pressure field.

### 3.2 Three-Dimensional Results

The disagreement of the total force data with the sectional estimates for the stationary cylinder highlights the need for a three-dimensional flow estimation procedure for full characterization of the forcing function acting on the cylinder. Figures 7, 8, and 9, summarise the results of the pseudo-instantaneous reconstructions for the stationary,  $2S$ , and  $2P_0$  cases, respectively. The methods are evaluated for their ability to estimate the instantaneous shedding phase variation along the span towards more accurate evaluation of total lift coefficient data from the PIV-based estimates.

Figures 7a, 8a, 9a, plot the reconstructed streamwise velocity fields at  $\hat{y} = 0.5$  by correlating the phase



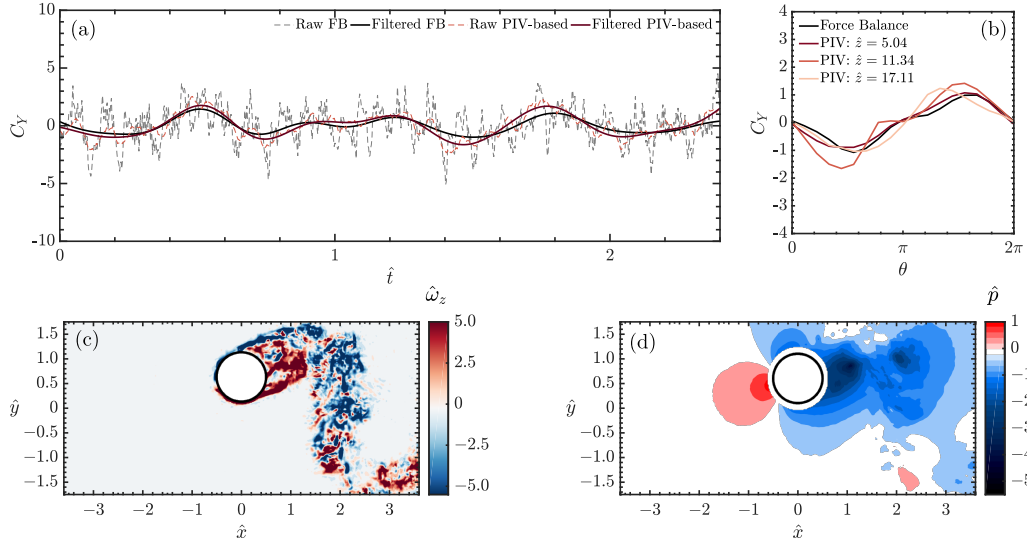


Figure 6: Sectional results for the oscillating cylinder at  $A^* = 0.8$ ,  $\lambda^* = 7.0$ . (a) Total lift coefficient force balance data compared to PIV-based sectional lift coefficient data, (b) phase averages of these data for each spanwise plane investigated, (c) instantaneous spanwise vorticity field and (d) instantaneous PIV-based pressure field.

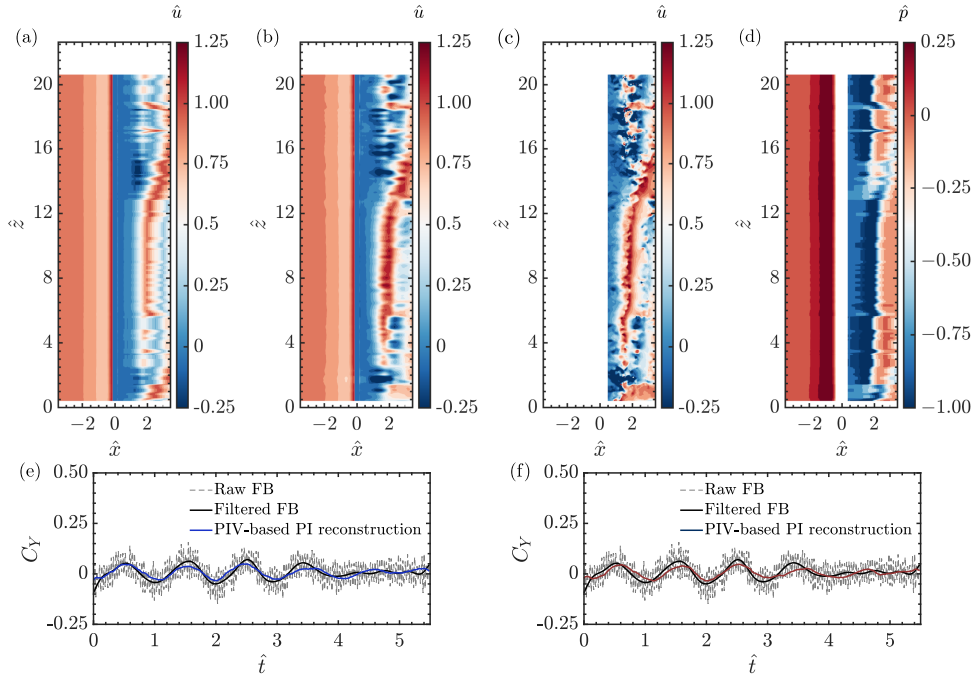


Figure 7: Stationary cylinder: reconstruction of instantaneous streamwise velocity at  $\hat{y} = 0.5$  using (a) phase-averaged method, (b) POD-based method, compared to (c) measured streamwise velocity data. (d) Reconstructed pressure at  $\hat{y} = 0.5$  using phase-averaged method. PIV-based total force reconstruction with (e) phase-averaged method and (f) POD-based method, compared to force balance data.

averaged velocity fields, obtained at the midspan of the cylinder ( $\hat{z} = 11.9$ ), to the instantaneous data, while figures 7b, 8b, and 9b plot the reconstructed steamwise velocity field at the same plane by projecting the instantaneous data onto the first 5 spatial POD modes to estimate the horizontal plane temporal coefficient data. When compared to the instantaneous vertical plane velocity field from which the reconstructions were

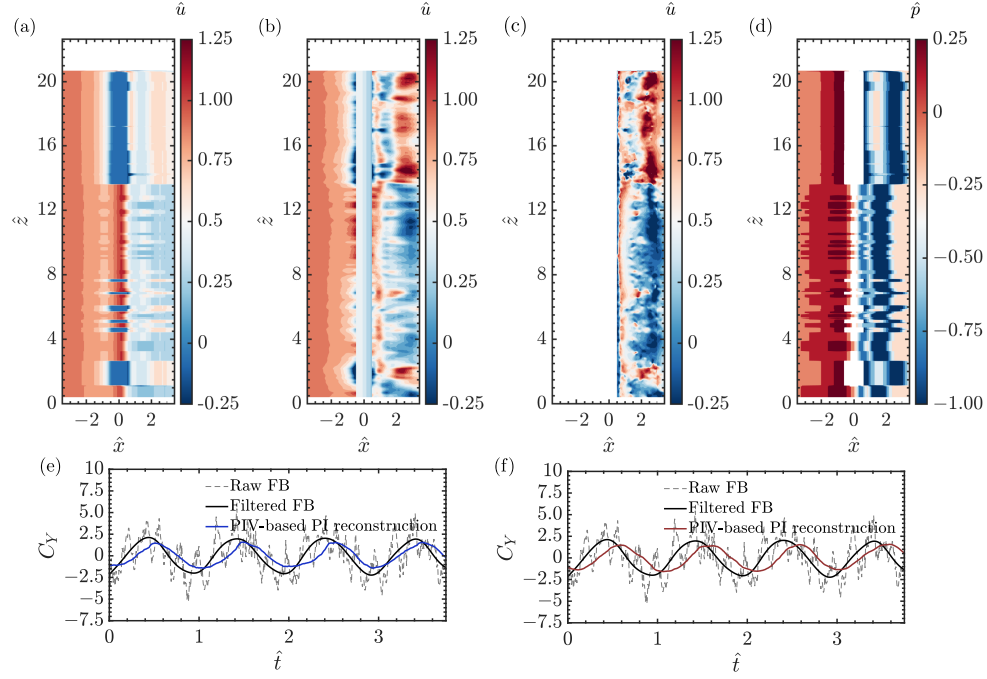


Figure 8: Oscillating cylinder at  $A^* = 0.45$ ,  $\lambda^* = 5.0$ : reconstruction of instantaneous streamwise velocity at  $\hat{y} = 0.5$  using (a) phase-averaged method, (b) POD-based method, compared to (c) measured streamwise velocity data. (d) Reconstructed pressure at  $\hat{y} = 0.5$  using phase-averaged method. PIV-based total force reconstruction with (e) phase-averaged method and (f) POD-based method, compared to force balance data.

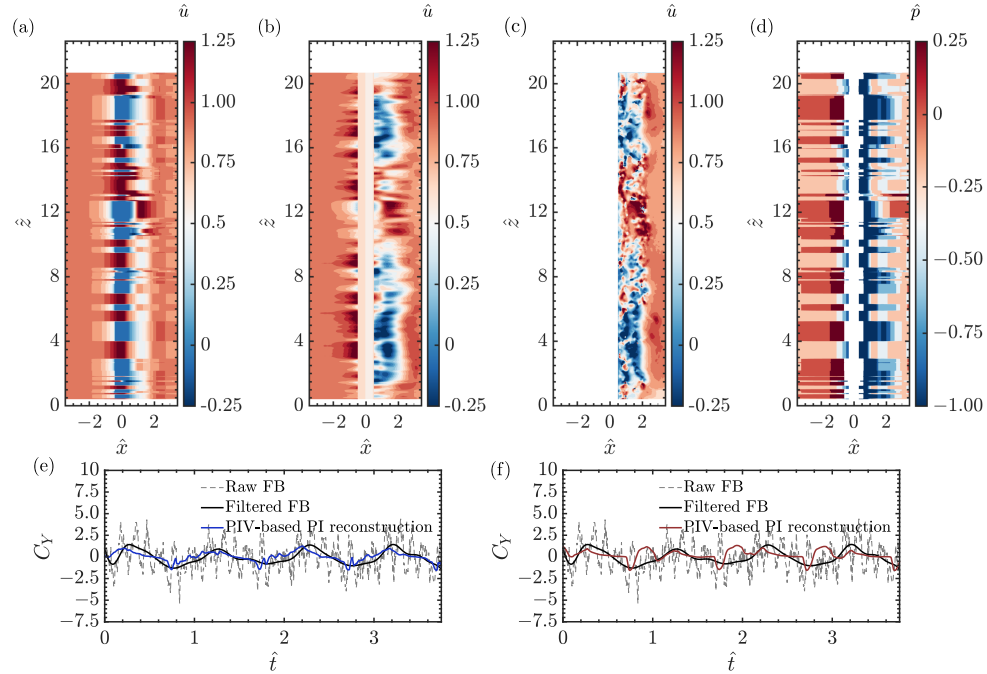


Figure 9: Oscillating cylinder at  $A^* = 0.8$ ,  $\lambda^* = 7.0$ : reconstruction of instantaneous streamwise velocity at  $\hat{y} = 0.5$  using (a) phase-averaged method, (b) POD-based method, compared to (c) measured streamwise velocity data. (d) Reconstructed pressure at  $\hat{y} = 0.5$  using phase-averaged method. PIV-based total force reconstruction with (e) phase-averaged method and (f) POD-based method, compared to force balance data.



derived (figures 7c, 8c, 9c), it can be observed that the low order representation constructed by projecting onto the first 5 spatial POD modes reconstructs the original field with a higher fidelity. When the shedding phase data ( $\theta(z, t)$ ) are estimated from the three-dimensional reconstructions using either the phase-averaged (figure 7e) or POD-based (figure 7f) methods for the stationary cylinder case, a substantial improvement in the alignment of both the phase and amplitude of the lift coefficient data between the force balance and PIV-based measurements is achieved compared to the previously discussed sectional measurements (figure 4a). Based on the reconstruction of the volumetric pressure field (figure 7d), the shedding of the vortex cores can be seen to vary in phase considerably over the length of the cylinder, resulting in the earlier observed changes in the phase of planar forcing along the span. However, in the sectional loading estimates discussed previously, significant modulations of the sectional fluctuating lift may occur on a cycle-to-cycle basis, indicating a more complex reconstruction may be required to correctly capture the dynamics associated with this modulation effect of the amplitude of the fluctuating lift at each spanwise location, instead of relying on a simple phase average based on the primary instability.

For the 2S and  $2P_0$  cases, the force reconstructions shows less agreement for both the phase-average and POD-based methods, with the POD-based method deteriorating substantially in the  $2P_0$  case. This appears to be due to the violation of the spanwise homogeneity of the data relied upon in order to apply the phase averaged fields or POD spatial modes corresponding to  $\hat{z} = 11.9$  at every spanwise position. Analysis of the instantaneous fields for the 2S case (figures 8a-d) reveals that, although the shedding remains locked in phase along the span, the vertical plane measurement gives drastically different streamwise velocity signatures at different spanwise locations. This is due to the expansion of the wake width with decreasing  $\hat{z}$ , such that the measurement plane cuts into the vortex core at some locations, but remains in the accelerated flow region outside the vortex core at other locations (i.e.,  $\hat{z} > 14$ ). This causes both methods to erroneously detect a phase switching in the shedding, resulting in an underprediction of the total lift coefficient amplitude and phase misalignment (figures 8e-f), compared to the previously observed good sectional force agreement. Similar issues are prevalent in the  $2P_0$  case, however, the wake width appears instead more narrow approaching the midspan. The resulting PIV-based total force reconstruction based on matching to sectional phase averaged fields maintains its phase relationship, however erroneous detection of phases contributes to higher noise levels (figure 9e).

## 4 Conclusions

A POD-based flow reconstruction technique is compared to a phase-averaged reconstruction technique for estimating total forcing on a three-dimensional bluff body from planar TR-PIV measurements for the case of a stationary, circular cylinder, and two oscillating cylinder case in 2S and  $2P_0$  shedding regimes in uniform cross flows. For the stationary cylinder case, the three-dimensional reconstruction techniques yield a substantial increase in correspondence with reference force balance measurements for determining the total instantaneous lift forcing acting on the cylinder, compared to corresponding PIV-based sectional force estimates. However, for the oscillating cylinder cases, the opposite is true. Since the phase of shedding is largely locked in along the span of the periodically oscillating cylinders, the sectional estimates instead show high correspondence with the reference force balance measurements, whereas the total force estimates based on the three-dimensional reconstructions are contaminated by errors associated with violations of the assumption of spanwise homogeneity of the flow statistics used to reconstruct the velocity fields. However, it is expected that more complex reconstruction methodologies will remedy these issues, such as linearly combining the POD modes and phase averaged fields from all three horizontal planes measured in order to best match the mean and fluctuating statistics at each spanwise position where the reconstruction and shedding phase is evaluated. In addition, reduction of the raw instantaneous vertical-plane fields using a reduced order model before use in reconstruction could yield some reduction in noise.

## Acknowledgements

The authors gratefully acknowledge the contribution of the Natural Science and Engineering Research Council (NSERC) to the funding of this research.

## References

- Bearman P (1984) Vortex shedding from oscillating bluff bodies. *Ann Rev Fluid Mech* 16:195–222
- Dabiri J (2005) On the estimation of swimming and flying forces from wake measurements. *Journal of Experimental Biology* 208:3519–3532
- de Kat R and van Oudheusden B (2012) Instantaneous planar pressure determination from PIV in turbulent flow. *Exp Fluids* 52:1089–1106
- Graham W, Pitt Ford C, and Babinsky H (2017) An impulse-based approach to estimating forces in unsteady flow. *J Fluid Mech* 815:60–76
- Guisart A, Bernal L, Dimitriadis G, and Terrapon V (2017) PIV-based estimation of unsteady loads on a flat plate at high angle of attack using momentum equation approaches. *Exp Fluids* 58:53
- Gurka R, Liberzon A, Hefetz D, Rubinstein D, and Shavit U (1999) Computation of pressure distribution using piv velocity data. in *3rd Int. Workshop on Particle Image Velocimetry*. pages 671–676. Santa Barbara
- Khalak A and Williamson C (1999) Motions, forces and mode transition in vortex-induced vibrations at low mass-damping. *J Fluid Struct* 13:813–851
- Limacher E, McClure J, Yarusevych S, and Morton C (2019) Comparison of momentum and impulse methods of force estimation using piv data. in *13th International Symposium on Particle Image Velocimetry*. Munich, Germany
- Limacher E, Morton C, and Wood D (2018) Generalized derivation of the added-mass and circulatory forces for viscous flows. *Phys Rev Fluids* 3:014701
- McClure J and Yarusevych S (2019) Planar momentum balance in three-dimensional flows: applications to load estimation. *Exp Fluids* 60:41
- McPhaden C and Rival D (2018) Unsteady force estimation using a Lagrangian drift-volume approach. *Exp Fluids* 59:64
- Morse T and Williamson C (2009) Prediction of vortex-induced vibration response by employing controlled motion. *Journal of Fluid Mechanics* 634:5–39
- Noack BR and Eckelmann H (2006) A global stability analysis of the steady and periodic cylinder wake. *Journal of Fluid Mechanics* 270:297–330
- Noca F, Shiels D, and Jeon D (1999) A comparison of methods for evaluating time-dependent fluid dynamic forces on bodies, using only velocity fields and their derivatives. *Journal of Fluids and Structures* 13:551–578
- Oudheusden B, Scarano F, Hinsberg N, and Watt D (2005) Phase resolved characterization of vortex shedding in the near wake of a square-section cylinder at incidence. *Experiments in Fluids* 39:86–98
- Riches G and Morton C (2018) One degree-of-freedom vortex-induced vibrations at constant Reynolds number and mass-damping. *Experiments in Fluids* 59:157
- Rival DE and van Oudheusden B (2017) Load-estimation techniques for unsteady incompressible flows.. *Exp Fluids* 58:20
- Sirovich L (1987) Turbulence and the dynamics of coherent structures, parts i-iii. *Quarterly of Applied Mathematics* 45:561590
- Spoelstra A, de Martino Norante L, Terra W, Sciacchitano A, and Scarano F (2019) On-site cycling drag analysis with the Ring of Fire. *Exp Fluids* 60:90
- Unal M, Lin J, and Rockwell D (1997) Force prediction by PIV imaging: a momentum-based approach. *Journal of Fluids and Structures* pages 965–971
- Wu J, Pan Z, and Lu X (2005) Unsteady fluid-dynamic force solely in terms of control-surface integral. *Physics of Fluids* 17:098102–1